





Magnetotransport signatures of chiral magnetic anomaly in the half-Heusler phase ScPtBiOrest Pavlosiuk ¹, Andrzej Jezierski ^{2,3}, Dariusz Kaczorowski ^{1,3} and Piotr Wiśniewski ^{1,*}¹*Institute of Low Temperature and Structure Research, Polish Academy of Sciences, ul. Okólna 2, 50-422 Wrocław, Poland*²*Institute of Molecular Physics, Polish Academy of Sciences, ul. M. Smoluchowskiego 17, 60-179 Poznań, Poland*³*Centre for Advanced Materials and Smart Structures, Polish Academy of Sciences, ul. Okólna 2, 50-422 Wrocław, Poland*

(Received 3 April 2020; revised 26 April 2021; accepted 28 April 2021; published 17 May 2021)

Study of the magnetotransport properties of ScPtBi revealed simultaneously (i) a negative contribution to the longitudinal magnetoresistance, (ii) the planar Hall effect, and (iii) distinct angular narrowing of the longitudinal magnetoresistance—three hallmarks of chiral magnetic anomaly (pumping of axial charge between Weyl nodes), a distinct property of topological semimetals. Electronic structure calculations show that structural defects, such as antisites and vacancies, bring a substantial density of states at the Fermi level of ScPtBi, indicating that it is a semimetal, not a zero-gap semiconductor, as predicted earlier. This is in accord with electrical resistivity in ScPtBi, showing no characteristics of a semiconductor. Moreover, below 0.7 K we observed an onset of a superconducting transition, with the resistivity disappearing completely below 0.23 K.

DOI: [10.1103/PhysRevB.103.205127](https://doi.org/10.1103/PhysRevB.103.205127)**I. INTRODUCTION****II. METHODS**

Chiral magnetic anomaly (CMA) is a unique and defining feature of topological semimetals due to charge pumping between Weyl nodes of opposite chirality. Weyl nodes are monopoles of Berry flux and possess characteristic chiral charge (or Chern number, being integral of the Berry flux through a closed surface enclosing the node), equal to ± 1 in a single-Weyl, or ± 2 in a double-Weyl semimetal [1].

CMA has three main electronic magnetotransport manifestations: negative longitudinal magnetoresistance (LMR) [2,3], the planar Hall effect (PHE), and angular narrowing of negative LMR [4,5]. All three have never been observed simultaneously in the same material. Negative LMR has been found in many topological semimetals, for example TaAs, TaP, ZrTe₅, Na₃Bi, GdPtBi, and YbPtBi [1,4,6–10]. PHE was observed less often, in Cd₃As₂, VAl₃, Na₃Bi, as well as half-Heusler phases GdPtBi, YbPtBi, and DyPdBi [10–15]. To date, angular narrowing of negative LMR has been found only in Na₃Bi [4].

ScPtBi, isostructural with GdPtBi, YbPtBi, and DyPdBi, but outstanding due to the very light and nonmagnetic scandium atom, factors important for the topological nontriviality of electronic states. It has been theoretically predicted to be a zero-gap semiconductor with inversion of electronic bands prerequisite for a \mathbb{Z}_2 -type topological insulator [16,17]. So far, only the observation of the weak antilocalization (WAL) effect and linear magnetoresistance suggested its topological nontriviality [18]. In this work, we synthesized the high-quality single crystals of ScPtBi and characterized them and their angle-dependent magnetotransport depending on the angle between current and applied magnetic field.

Single crystals of ScPtBi were grown by the self-flux method from high-purity constituent elements (Sc 3N, Pt 5N, Bi 6N) taken in the atomic ratio Sc:Pt:Bi as 1:1:15, put in an alumina crucible, and sealed in a quartz ampule with argon pressure of 0.3 bar. Such a prepared ampule was quickly heated up to 1150 °C at a rate of 50 °C/h and held at this temperature for 24 h. Then it was slowly cooled down to 700 °C at a rate of 1 °C/h, and the excess of Bi-flux was removed by centrifugation. Obtained single crystals were pyramid-shaped and stable against air and moisture. The largest of them had dimensions of 6×3×3 mm³ (see the right inset in Fig. S1 in the Supplemental Material [19]).

The equiatomic chemical composition and phase homogeneity of crystals were confirmed by energy-dispersive x-ray analysis using an FEI scanning electron microscope equipped with an EDAX Genesis XM4 spectrometer (Fig. S1 of the Supplemental Material [19]). X-ray powder diffraction experiment was carried out on powdered single crystals using an X'pert Pro (PANalytical) diffractometer with Cu $K\alpha$ radiation. Crystal structure refinement by the Rietveld method was performed with the FULLPROF package [20] (a diffractogram and the results of the refinement are shown in Fig. S2A and Table S1 of the Supplemental Material [19]). The results of analysis indicated that ScPtBi crystallizes within the $F\bar{4}3m$ space group with the lattice parameter $a = 6.4412$ Å, which differs very slightly from $a = 6.50$ Å reported in Ref. [18]. The quality and orientation of single crystals were assessed by Laue diffraction, with a LAUE-COS (Proto) system (the Laue pattern is shown in Fig. S2B of the Supplemental Material [19]). A bar-shaped (0.19×0.65×1.73 mm³) specimen was cut from the oriented single crystal. A conventional four-probe method was used for electrical transport measurements in the temperature range from 0.05 to 300 K and in magnetic fields up to 14 T, using a PPMS platform (Quantum Design) equipped with a dilution refrigerator. Electrical contacts were

*Corresponding author: p.wisniewski@intibs.pl

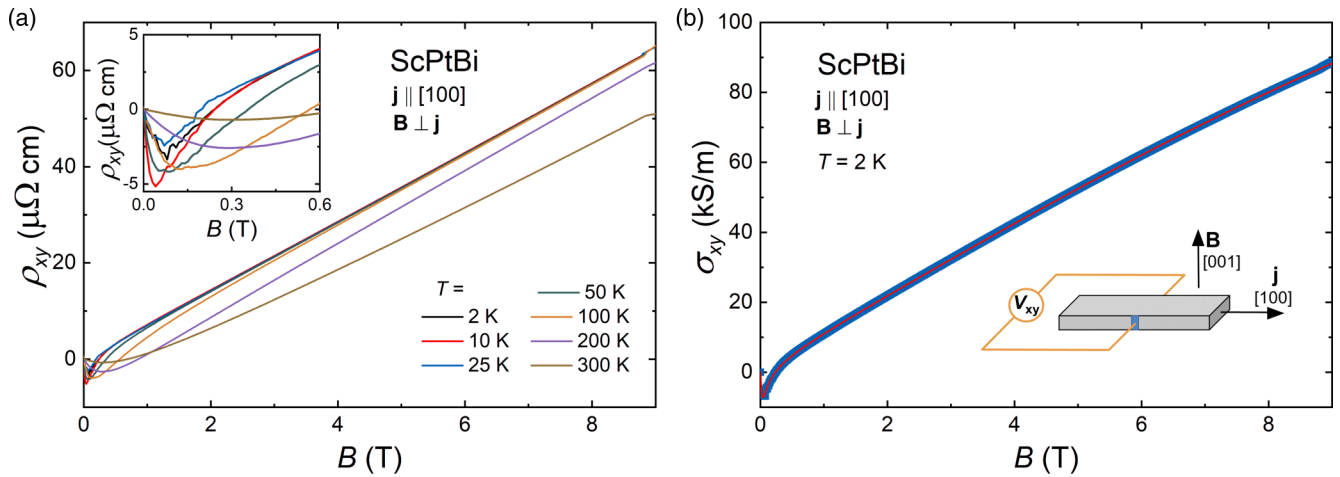


FIG. 1. (a) Hall resistivity measured at several different temperatures as a function of magnetic field with $\mathbf{j} \parallel [100]$ and $\mathbf{B} \parallel [001]$. The inset presents the Hall resistivity in the weak magnetic field region. (b) Magnetic-field-dependent Hall conductivity measured at $T = 2$ K. The red solid line represents the fit with Eq. (1). The quality of the fit was excellent (with $R^2 > 99.99$). The inset shows the geometry of measurement.

made from 50- μm -thick silver wires attached to the sample with silver paint. We took special care while preparing the contacts to avoid current jetting, which could cause spurious negative LMR, as described in Refs. [13,15]. The same PPMS platform was used for specific-heat measurements.

The electronic structure was calculated by the full-potential local orbital minimum basis (version 18) method [21,22] in the local density approximation, with the exchange correlation potential taken in the form of Perdew, Burke, and Ernzerhof (PBE) [23]. The band structure of the ordered ScPtBi was calculated in the full-relativistic mode in the general gradient approximation, including the spin-orbit interaction. For the disordered structures and for models with vacancies, the band calculations were performed for a supercell of 24 atoms ($\text{Sc}_8\text{Pt}_8\text{Bi}_8$) in the full-relativistic and scalar-relativistic schemes, respectively. In the antisite models, we interchanged two atoms from two different sublattices, per supercell. In the models with vacancies, one of the atoms (Sc, Pt, or Bi) was vacant per supercell.

III. RESULTS AND DISCUSSION

Contrary to prior theoretical predictions [16,17], our ScPtBi samples exhibited a metalliclike temperature dependence of electrical resistivity, ρ_{xx} , shown in Fig. S4A of the Supplemental Material [19]. Moreover, zooming into the low-temperature region, we observed below 0.7 K an onset of a superconducting transition, with ρ_{xx} finally decreasing to zero below 0.23 K (see the inset to Fig. S4A of the Supplemental Material [19]).

The Hall resistivity isotherms, $\rho_{xy}(B)$, are nonlinear, especially in weak magnetic fields, where they have minima, indicating two or more different bands contributing to ρ_{xy} [Fig. 1(a) and its inset; raw data before antisymmetrization are shown in Fig. S5 of the Supplemental Material [19]]. Previously reported rectilinear $\rho_{xy}(B)$ data for ScPtBi showed only one type of carrier contributing to the transport properties [18], suggesting different electronic structures of our samples. Nonlinear $\rho_{xy}(B)$ have also been observed for several half-Heusler compounds: YbPtBi, LuPtBi, YPtBi, TbPdBi, and

DyPdBi [15,24–27]. Therefore, for a quantitative analysis of our data, we used the three-band (the two-band model was tested as well, but it did not fit our data) Drude model of Hall conductivity:

$$\sigma_{xy}(B) = \sum_{i=1}^3 \frac{e n_i \mu_i^2 B}{1 + (\mu_i B)^2}, \quad (1)$$

summing up the conductivities of individual bands, with n_i and μ_i denoting, respectively, the concentration and mobility of carriers from the i th band (e is the elementary charge). We fitted Eq. (1) to the experimental Hall conductivity data calculated as $\sigma_{xy} = \rho_{xy}/(\rho_{xx}^2 + \rho_{xy}^2)$, appropriate because $\rho_{xy} \ll \rho_{xx}$. The result of Eq. (1) fitting to $\sigma_{xy}(B)$ obtained at $T = 2$ K is represented by a red solid line in Fig. 1(b). The same Eq. (1) was fitted to the $\sigma_{xy}(B)$ data measured at other temperatures; the results are shown in Fig. S6 [19], and fit parameters are collected in Table S2 [19].

Interestingly, charge mobilities derived for two of these bands are very high, especially that of an electronlike band: $\mu_2 \approx 2 \times 10^5 \text{ cm}^2 \text{ V}^{-1} \text{ s}^{-1}$, which is the highest ever observed for pnictogen-bearing half-Heusler phases, and similar to those in topological semimetals ZrTe₅ [28], TaAs [29], and WTe₂ [30].

Looking for topological semimetal features in ScPtBi, we measured its ρ_{xx} as a function of magnetic field, B , and calculated the magnetoresistance, $\text{MR} = [\rho_{xx}(B)/\rho_{xx}(0)] - 1$, for different angles θ between \mathbf{B} and electric current \mathbf{j} [as shown in Fig. 2(a) for $T = 2$ K]. MR is the largest in transverse configuration (TMR), i.e., with $\mathbf{B} \perp \mathbf{j}$. When \mathbf{B} is rotated [$\theta = 90^\circ \rightarrow 0^\circ$, as sketched in the inset to Fig. 2(a)], MR decreases monotonously, down to the lowest value in an LMR configuration ($\theta = 0^\circ$). The field variation of LMR at 2 K is fairly unusual: it increases abruptly with increasing B , reaches a maximum of 64% in 2.75 T, and decreases gradually in stronger fields.

The magnetic field dependence of LMR changes prominently with temperature [Fig. 2(b)]. The negative slope of LMR(B) at $T = 2$ K gradually becomes positive as temperature increases. This behavior can be ascribed to the presence

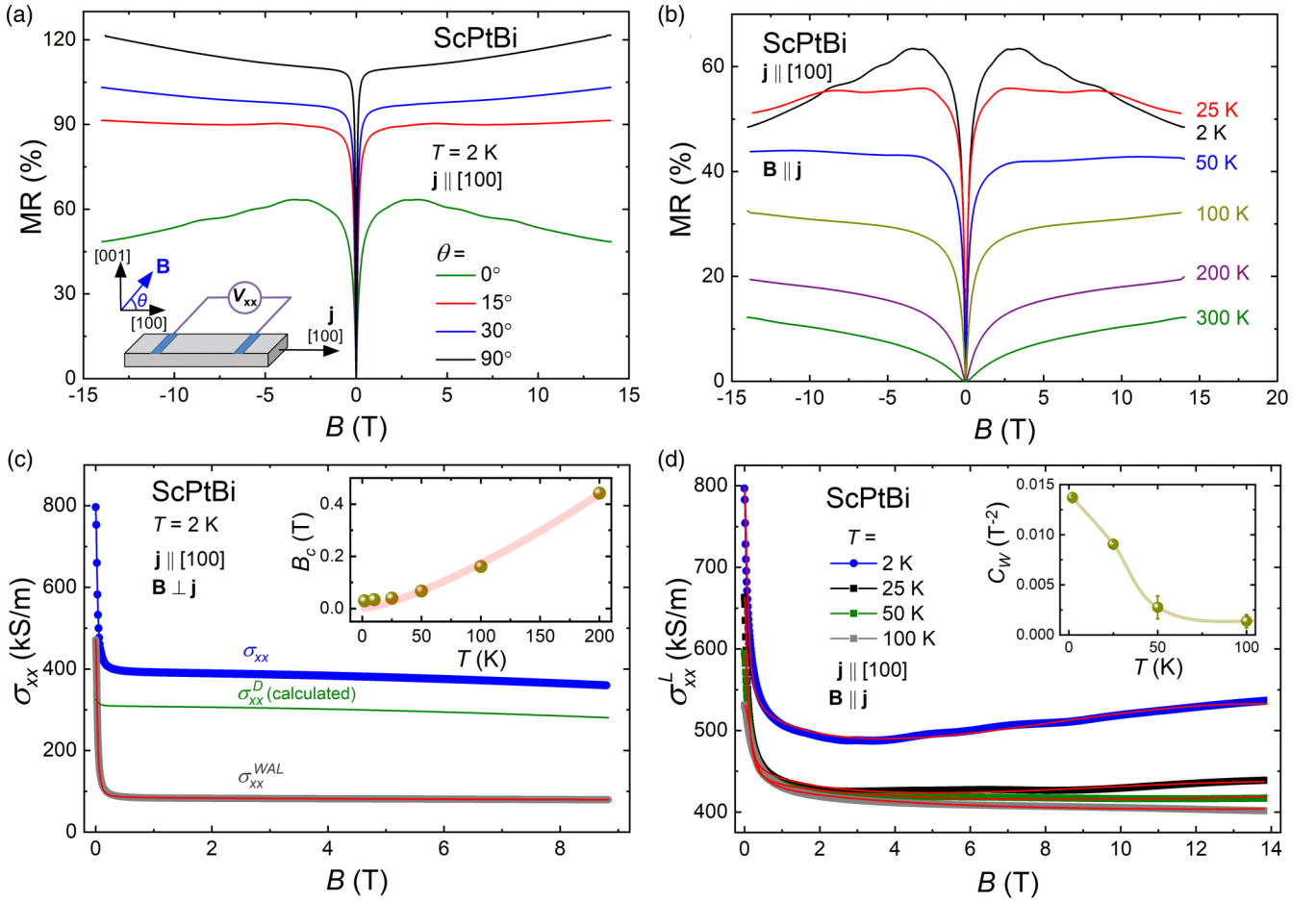


FIG. 2. (a) MR(B) isotherms measured at $T = 2$ K for different angles between current and magnetic field. The inset shows schematically the geometry of measurement. (b) LMR(B) isotherms for several temperatures. (c) Analysis of the transverse magnetoconductivity data obtained at $T = 2$ K. Blue points, experimental data; green solid line, $\sigma_{xx}^D(B)$ calculated with Eq. (2). The gray solid curve represents the WAL contribution derived as described in the text, and the red solid curve shows the fit of Eq. (3). Inset: temperature dependence of the critical field approximated by power law $B_c \propto T^{1.35}$. (d) Magnetic field dependence of the longitudinal magnetoconductivity for several temperatures. Red solid lines correspond to the fits of Eq. (4). Inset: temperature-dependent chiral coefficient (the solid line is a guide for the eye).

of at least two contributions: increasing-in-field (dominating in weak fields) and decreasing-in-field (taking over in stronger fields).

Finite LMR has been observed for many compounds, and when positive, it can be ascribed to anisotropic scattering [31] or anisotropy of the Fermi surface [32]. Also macroscopic inhomogeneities may lead to positive or negative LMR [33], but they are absent in our samples (Fig. S1 [19]). LMR in topological semimetals is characterized by a distinct, additional negative contribution from CMA [3]. Therefore, we analyzed LMR in ScPtBi to check for its presence.

MR measured for ScPtBi in both the transverse and longitudinal configuration demonstrates a very sharp increase in the weak magnetic field region [Fig. 2(a)], which can be ascribed to WAL [18]. In stronger fields, the increase of TMR becomes much slower. To describe this complex variation of TMR, we combined a WAL contribution with three-band Drude magnetoconductivity calculated as

$$\sigma_{xx}^D(B) = \sum_{i=1}^3 \frac{e n_i \mu_i}{1 + (\mu_i B)^2}, \quad (2)$$

using the concentrations and mobilities of charge carriers obtained in the analysis of Hall resistivity (cf. Table S2 [19]). $\sigma_{xx}^D(B)$ for 2 K is drawn in Fig. 2(c) as a green solid line. Next, we subtracted $\sigma_{xx}^D(B)$ from the transverse electrical magnetoconductivity $\sigma_{xx} [= \rho_{xx}/(\rho_{xx}^2 + \rho_{xy}^2)]$ (blue points). In this way, we obtained the WAL contribution σ_{xx}^{WAL} to TMR in ScPtBi, shown in Fig. 2(c) as a gray solid line. Remarkably, we could very well approximate it with the equation proposed to describe WAL in Weyl semimetals:

$$\sigma_{xx}^{\text{WAL}}(B) = C_1^{qi} \frac{B^2 \sqrt{B}}{B_c^2 + B^2} + C_2^{qi} \frac{B_c^2 B^2}{B_c^2 + B^2} + \sigma_0, \quad (3)$$

where σ_0 is the electrical conductivity in zero magnetic field, and B_c stands for the critical field related to the phase coherence length, l_ϕ , as $B_c \sim \hbar/(e l_\phi^2)$ [34]. Fitting this equation to σ_{xx}^{WAL} data [as shown by the red line in Fig. 2(c)], we obtained the parameters listed in Table S3A [19].

According to Ref. [34], at low temperatures the low-field magnetoconductivity is proportional to $+\sqrt{B}$ in double-Weyl

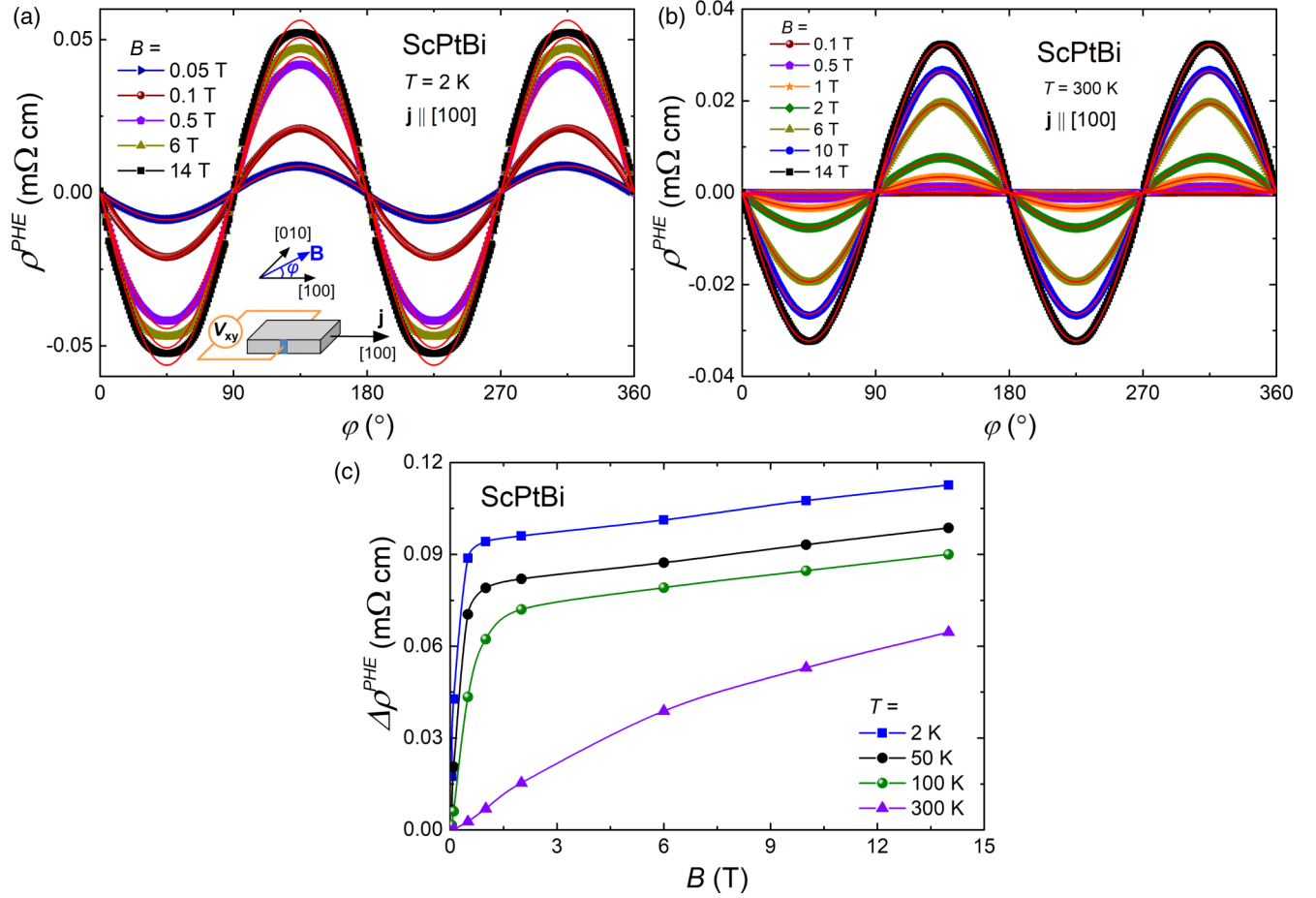


FIG. 3. Angular dependence of the planar Hall resistivity measured in different external magnetic fields at 2 K (a) and 300 K (b), with experimental geometry sketched in the inset to panel (a). Red solid lines represent the fits obtained using Eq. (5). (c) Magnetic field variations of the PHE magnitude observed at several different temperatures. Lines are guides for the eye.

semimetals and to $-\sqrt{B}$ in single-Weyl semimetals. For σ_{xx} of our sample at $T = 2$ K, the critical field, B_c , is very small (0.029 T in Table S3), thus the first term of Eq. (3) is very well approximated with $C_1^{qi}\sqrt{B}$. Therefore (since $C_1^{qi} < 0$), the low-field σ_{xx} is proportional to $-\sqrt{B}$, which allows us to conclude that ScPtBi is a single-Weyl semimetal.

The analysis of WAL that we performed for TMR at higher temperatures is shown in Fig. S7 and Table S3 of the Supplemental Material [19]. The temperature variation of critical field B_c , shown in the inset to Fig. 2(c), can be well approximated with a power law $B_c = AT^p$, with $A = 3.47 \times 10^{-4}$ T/K and $p = 1.35$. This value of p is close to 1.5, the theoretical value for electron-electron interaction, the principal mechanism of decoherence, indicating that our estimation of the WAL contribution is adequate.

In single-Weyl semimetals, WAL is isotropic [35], contributing to both longitudinal and transverse magnetoconductivity in the same way. The Lorentz force acting on electrons in parallel magnetic and electric fields is zero, hence LMR is not affected by orbital magnetoresistance [32]. Thus only contributions from WAL and CMA must be taken into account. We obtained the longitudinal magnetoconductivity $\sigma_{xx}^L(B)$ in ScPtBi as the inverse of the electrical resistivity measured in a longitudinal magnetic field: $\sigma_{xx}^L(B) = 1/\rho_{xx}(B)|_{\mathbf{B}||\mathbf{j}}$ [plotted in

Fig. 2(d)]. Fitting these data with the formula appropriate for Weyl semimetals [36],

$$\sigma_{xx}^L = \sigma_{xx}^{\text{WAL}}(B)(1 + C_W B^2) + \sigma_n \quad (4)$$

[represented by red solid lines in Fig. 2(d)], where $\sigma_n = \sigma_{xx}^L(B=0) - \sigma_0$, gave the parameters gathered in Table S3B [19]. This analysis reveals that the negative contribution to LMR that we observed may be due to CMA. It weakens with increasing temperature, as reflected by the decrease of the chiral coefficient, C_W [cf. the inset to Fig. 2(d)]. The chiral coefficient that we derived (0.015 T^{-2} at 2 K) is small, but very close to 0.021 T^{-2} observed in isostructural YbPtBi, a well-established topological semimetal [10].

Next, we performed measurements of another indicator of CMA: the planar Hall resistivity, ρ^{PHE} , in the geometry shown in the inset to Fig. 3(a). The magnetic field was always in the plane of the sample; the voltage drop was recorded as a function of the angle between magnetic field and current direction, ϕ . ρ^{PHE} depends on angle ϕ as follows [5,32]:

$$\rho^{\text{PHE}}(\phi) = -\Delta\rho^{\text{PHE}} \sin 2\phi, \quad (5)$$

where $\Delta\rho^{\text{PHE}}$ stands for the magnitude of the PHE. We found that the behavior of $\rho^{\text{PHE}}(\phi)$ in ScPtBi is typical, and it persists in temperatures up to 300 K [Fig. 3(b)].

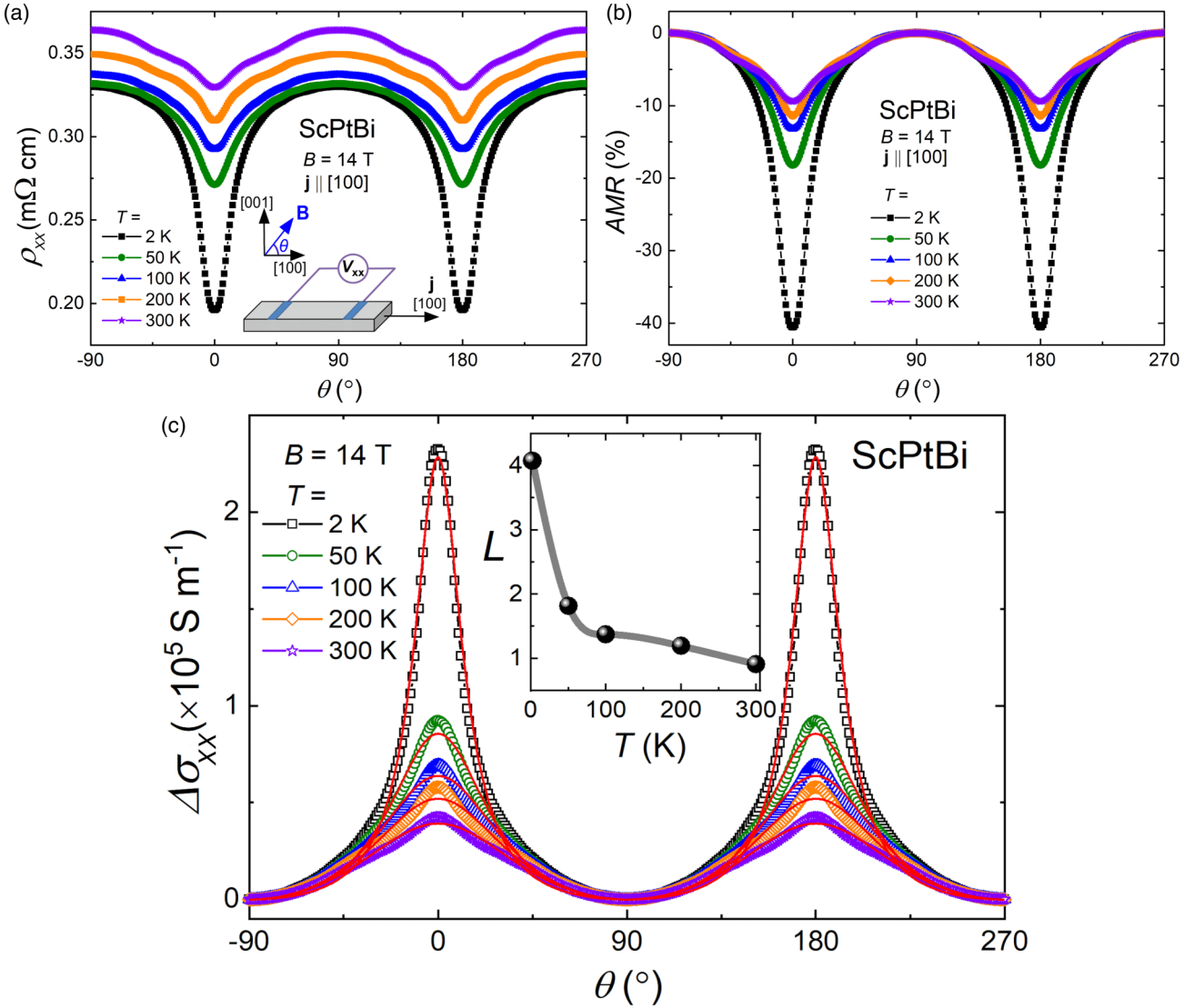


FIG. 4. (a) Angular dependence of the electrical resistivity measured at several temperatures in a magnetic field of 14 T. The inset shows the geometry of measurement. (b) Anisotropic magnetoresistance isotherms calculated from the data presented in (a). (c) Conductivity enhancement derived from the data shown in (a). Red lines represent the results of fitting Eq. (6) to the experimental data. The inset displays the temperature dependence of the narrowing parameter L defined in the text. The solid line is a guide for the eye.

Remarkably, PHE in ScPtBi is discernible even in very weak magnetic fields: $B = 0.05$ T at $T = 2$ K [see Fig. 3(a)] and $B = 0.1$ T at $T = 300$ K [Fig. 3(b)], indicating this material as a possible directional magnetic field sensor. $\Delta\rho^{\text{PHE}}$ measured for ScPtBi increases with increasing the strength of the applied magnetic field and decreases with increasing temperature, which is summarized in Fig. 3(c). The magnitude of PHE in ScPtBi is smaller than that reported for other half-Heusler compounds [14,15], but larger than that observed for VAl_3 or WTe_2 [12,37].

The observation of PHE cannot be considered as sufficient proof of the existence of CMA, because any material that demonstrates anisotropic magnetoresistance (AMR) also shows PHE. AMR can have several different origins: ferromagnetism, Fermi surface anisotropy [32], and/or CMA [2,3]. In ferromagnets, AMR depends on θ as $\cos^2\theta$, while in materials with a quasi-2D Fermi surface it depends on θ as $|\cos\theta|$ [32], where θ is the angle between \mathbf{B} and \mathbf{j} .

In the presence of CMA, PHE must be accompanied by negative LMR and a particular angular dependence of AMR (also called angular narrowing of LMR) [5]. According to Burkov, the conductivity enhancement defined as $\Delta\sigma_{xx} \equiv \rho_{xx}^{-1}(\theta) - \rho_{xx}^{-1}$ [where $\rho_{xx}^{-1} \equiv \rho_{xx}(90^\circ)$] should depend on θ in the following way:

$$\Delta\sigma_{xx} \propto \frac{L^2 \cos^2 \theta}{1 + L^2 \sin^2 \theta}, \quad (6)$$

with $L = L_c/L_a$, where L_c is the chiral charge diffusion length, and L_a is the magnetic field related length scale [5].

Thus, we measured ρ_{xx} of ScPtBi as a function of θ in constant field $B = 14$ T at temperatures in the range from 2 to 300 K [see Fig. 4(a)]. Next we calculated $\text{AMR} = [\rho_{xx}(\theta) - \rho_{xx}(90^\circ)]/\rho_{xx}(90^\circ)$, which is plotted in Fig. 4(b), and obviously follows neither $\cos^2\theta$ nor $|\cos\theta|$.

However, the model proposed by Burkov [5] does not include the WAL contribution to conductivity, which, as

we showed above, is important in ScPtBi. Because in single-Weyl SMs σ_{xx}^{WAL} is isotropic [35], it will cancel out in $\Delta\sigma_{xx}(\theta)$ defined just as a difference of conductivities: $\sigma_{xx}(\theta) - \sigma_{xx}(90^\circ)$. Consequently, we calculated $\sigma_{xx}(\theta) = \rho_{xx}(\theta)/[\rho_{xx}^2(\theta) + \rho_{xy}^2(\theta)]$, using $\rho_{xx}(\theta)$ measured in a field of 14 T [black symbols in Fig. 4(a)] and $\rho_{xy}(\theta) = \rho_{xy}(14 \text{ T}) \sin \theta$, where $\rho_{xy}(14 \text{ T})$ were extrapolated linearly to $B = 14 \text{ T}$, values of $\rho_{xy}(B)$ measured at each temperature [shown in Fig. 1(a)].

We fitted Eq. (6) to all $\Delta\sigma_{xx}(\theta)$ isotherms, as shown by red solid lines in Fig. 4(c). The very good fit obtained for the data collected at $T = 2 \text{ K}$ confirms the angular narrowing of LMR, and therefore the presence of CMA in ScPtBi.

The fit parameter L “determines the strength of the chiral anomaly induced magnetotransport effects” [5]. It is the ratio of two length parameters: $L_c = \sqrt{D\tau_c}$ and $L_a = D/(\Gamma B)$, where D is the diffusion coefficient of carriers (increasing with T), Γ is a parameter inversely proportional to the density of states at the Fermi level (nearly T -independent), and τ_c is the chiral charge relaxation time, slowly (because of topological protection and conservation of chiral charge) decreasing with temperature. Therefore, $L = (L_c/L_a) \propto 1/\sqrt{D}$ should decrease with increasing temperature, as is indeed shown in the inset to Fig. 4(c).

With increasing temperature, the quality of the fitting worsens, as the contribution of CMA to LMR is reduced, which is reflected in a decrease of the fitted parameter L , $\Delta\rho^{\text{PHE}}(T)$ [Fig. 3(c)], and $C_W(T)$ [inset to Fig. 2(d)].

The values and form of $\Delta\sigma_{xx}(\theta)$ that we observed are very similar to those reported for the Weyl semimetal Na_3Bi [4], which further supports the presence of topologically nontrivial electronic structure in ScPtBi.

A. Electronic structure calculations

Earlier electronic structure calculations have suggested that ScPtBi is a zero-gap semiconductor with inverted bands near the center of the Brillouin zone, where the gap closes [16,17], similar to that of GdPtBi [7]. Recently, qualitatively similar electronic band structure has been calculated by Majumder and Mitro [38].

We got very similar results for a model with perfectly ordered ScPtBi crystal structure. The obtained band structure is shown in Fig. 5(a), and the density of states (DOS) as a function of energy has zero value at the Fermi level, as shown in Fig. 5(b). This structure is, however, in disagreement with our experimental data (metalliclike resistivity (Fig. S4A) and specific-heat analysis in the Supplemental Material [19]), which directly point to a substantial DOS at the Fermi level (E_F).

There has recently been proposed a model of half-Heusler crystal structure with a Pt atom in Wyckoff position $4c$ ($1/4, 1/4, 1/4$) split in the randomly quarter-occupied $16e$ position (x, x, x) [39]. Refinement of the x-ray diffraction pattern revealed that this model describes the structure of our ScPtBi crystals as well as the model of an ideal half-Heusler (cf. Table S1 [19]). We incorporated this model in our electronic structure calculations and found that the relatively big change of Pt position (to $x = 0.2$, i.e., 0.05 shift from $4c$) results in a finite $\text{DOS}(E_F)$ equal to 0.069 st./(eV f.u.) [see Figs. 5(c)

and 5(d)]. Our ScPtBi crystal structure refinement (Table S1) using that model gave $x = 0.242$ for the $16e$ position of Pt atoms, i.e., only 0.008 deviation from $x = 1/4$ of the $4c$ position, much smaller than needed to sufficiently affect the DOS. Therefore, this model alone does not suffice to explain the semimetallic nature of ScPtBi. Interestingly, the band structure for this model contains three bands crossing the Fermi level, and a gap (of $\approx 50 \text{ meV}$) between inverted bands, where Dirac points may occur [marked with a red ellipse in Fig. 5(c)], indispensable for realization of the Weyl semimetal.

GdPtBi is a Weyl semimetal with Weyl nodes induced by an external magnetic field. The magnetic field is not taken into account in *ab initio* band-structure calculations (showing a zero-gap semiconductor), and in zero-field, GdPtBi does not show metallic $\rho_{xx}(T)$ [7]. Therefore, it is the influence of the magnetic field on the electronic structure, acting as a source of finite $\text{DOS}(E_F)$, that is a prerequisite to a semimetallic state [7]. For ScPtBi, metalliclike $\rho_{xx}(T)$ is observed even in zero magnetic field, which allows us to discard that scenario.

The ideal half-Heusler structure consists of three sublattices, each fully occupied by atoms of only one kind. But in real, even apparently perfect single crystals, different defects, such as antisites or vacancies, always occur. Thus, we examined if structural defects can be alternative sources of finite $\text{DOS}(E_F)$ in ScPtBi.

Calculations for models of ScPtBi with different antisites indeed brought finite $\text{DOS}(E_F)$ [see Fig. 5(c)] and thus profound changes in the electronic structure. For one Sc-Bi antisite per supercell, $\text{DOS}(E_F)$ is 0.83 st./(eV f.u.), for a Sc-Pt antisite: 0.60 st./(eV f.u.), and for Pt-Bi: 0.58 st./(eV f.u.), where f.u. stands for formula unit. Vacancies also lead to nonzero values of $\text{DOS}(E_F)$. One Pt or Bi vacancy per supercell yielded the DOS shown in Fig. 5(f), which at the Fermi level has values of 0.67 and 0.57 st./(eV f.u.), respectively (but zero for a Sc vacancy).

All these finite $\text{DOS}(E_F)$ values are significantly larger than 0.09 st./(eV f.u.) obtained from the specific-heat results (shown in the Supplemental Material [19]), most likely due to the smaller degree of disorder in our real crystal than that assumed in the models tested. However, regardless of antisite type, and for Pt or Bi vacancies, as well as for the structure with Pt occupying the $16e$ Wyckoff position, we always obtained semimetallic electronic structure. Additionally, in all these cases, the Fermi level crosses both hole- and electronlike bands (Fig. 5(c) and Fig. S8 [19]), which is in agreement with the results of our Hall resistivity measurements (Fig. 1 and Table S2 [19]). Thus, both antisites and vacancies may be important sources of nonvanishing DOS at the Fermi level in ScPtBi, and very likely also in other half-Heusler semimetals. Our calculations for antisite vacancies did not reveal features of topological semimetal close to E_F , but those for the structure with Pt at the $16e$ position revealed a gap between inverted bands where Dirac points might occur. ScPtBi may become a Weyl semimetal upon application of a magnetic field, splitting such Dirac points into two Weyl nodes, like in Na_3Bi or GdPtBi. Xiong *et al.* proposed that the Zeeman interaction is responsible for such a splitting in Na_3Bi [4], whereas for GdPtBi, both the Zeeman effect [7] and,

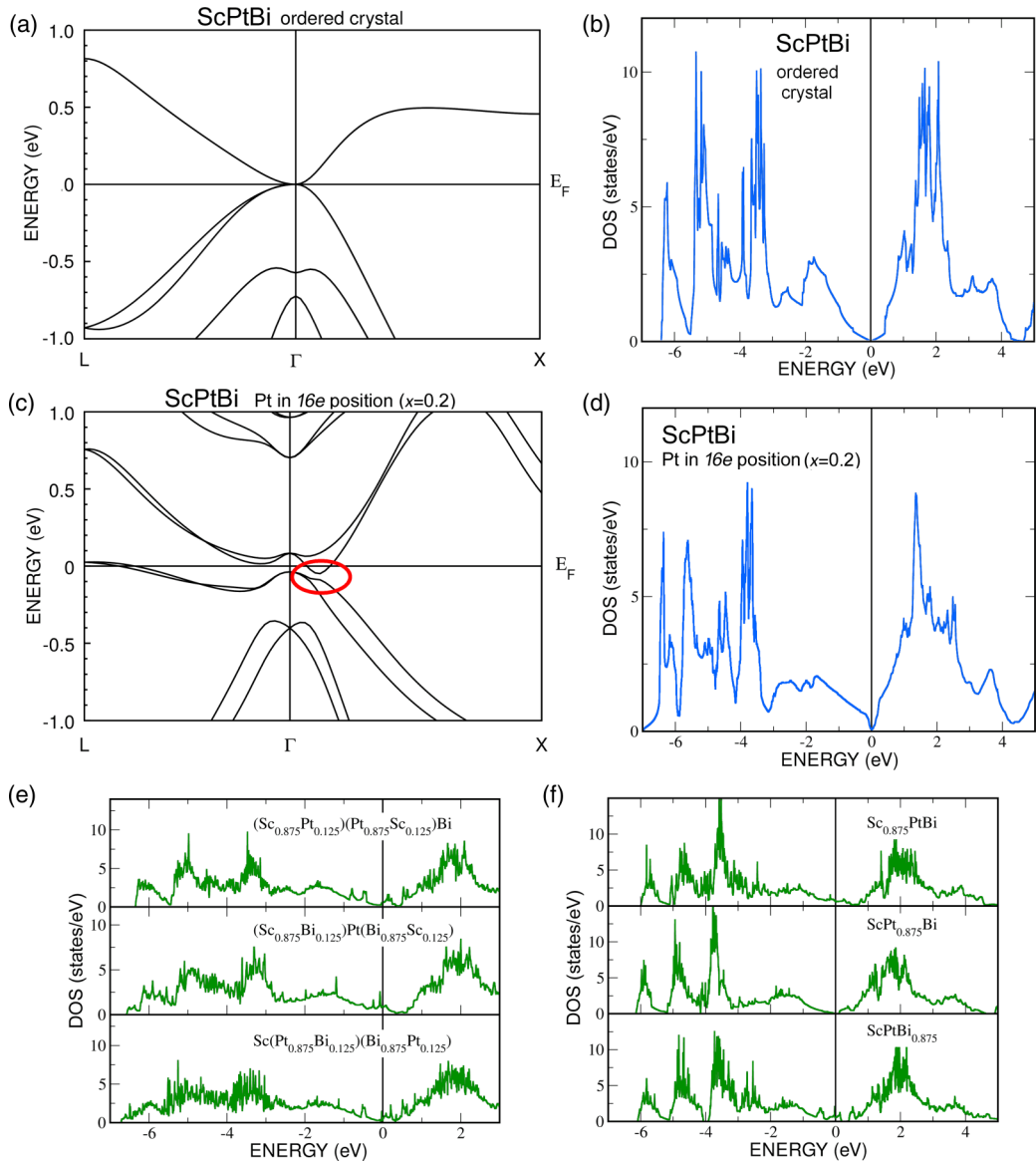


FIG. 5. (a) Band structure and (b) total DOS calculated (including spin-orbit interaction) for the ideal crystal structure of ScPtBi. (c) Band structure and (d) total DOS calculated (including spin-orbit interaction) for the model with Pt occupying the 16e Wyckoff position. The red ellipse in (c) marks a gap between inverted bands where Dirac points may occur. (e), (f) Total DOS for models: (e) with different antisites, and (f) with different vacancies.

alternatively, the exchange field due to the magnetic moments of Gd [40] have been suggested as direct causes of the formation of Weyl nodes. In the case of ScPtBi, despite being isostructural with GdPtBi, the absence of atoms with strong magnetic moments leads to exclusion of the exchange field, and it points to Zeeman splitting as the origin of Weyl nodes.

IV. CONCLUSION

Our examination of magnetotransport in ScPtBi revealed nonlinear Hall resistivity and large, positive, and nonsaturating TMR. Fitting the three-band Drude model to those data indicated ultrahigh carrier mobility in one of the bands. The low-field behavior of TMR could be well modeled with a WAL contribution.

Importantly, upon rotation of the sample in magnetic field, passing from a transverse to a longitudinal configuration, the slope of $MR(B)$ changes from positive to negative (in fields above 3 T). This reflects the significant negative component in LMR, a basic hallmark of CMA. Moreover, we observed in our sample two other crucial signs of CMA, namely the planar Hall effect and angular narrowing of negative LMR. With increasing temperature, particular parameters of all these properties—the chiral coefficient in longitudinal magnetoconductance, the magnitude of the PHE, and the chiral charge diffusion length—clearly diminished, reflecting weakening of the CMA effect. Our analysis indicates that ScPtBi is a single-Weyl semimetal.

Our unique observation of all three hallmarks of CMA simultaneously in one material allows us to conclude that ScPtBi is the new representative of topological semimetals.

The superconductivity we observed in ScPtBi makes this system even more interesting and worth further studies, due to conjunction with topologically nontrivial states, which may be important for quantum computing.

ACKNOWLEDGMENT

Work was supported by the National Science Centre of Poland (2015/18/A/ST3/00057 to D.K. and P.W.), and the Foundation for Polish Science (START 66.2020 to O.P.).

- [1] N. P. Armitage, E. J. Mele, and A. Vishwanath, *Rev. Mod. Phys.* **90**, 015001 (2018).
- [2] H. Nielsen and M. Ninomiya, *Phys. Lett. B* **130**, 389 (1983).
- [3] D. T. Son and B. Z. Spivak, *Phys. Rev. B* **88**, 104412 (2013).
- [4] J. Xiong, S. K. Kushwaha, T. Liang, J. W. Krizan, M. Hirschberger, W. Wang, R. J. Cava, and N. P. Ong, *Science* **350**, 413 (2015).
- [5] A. A. Burkov, *Phys. Rev. B* **96**, 041110(R) (2017).
- [6] X. Huang, L. Zhao, Y. Long, P. Wang, D. Chen, Z. Yang, H. Liang, M. Xue, H. Weng, Z. Fang, X. Dai, and G. Chen, *Phys. Rev. X* **5**, 031023 (2015).
- [7] M. Hirschberger, S. Kushwaha, Z. Wang, Q. Gibson, S. Liang, C. A. Belvin, B. A. Bernevig, R. J. Cava, and N. P. Ong, *Nat. Mater.* **15**, 1161 (2016).
- [8] C.-L. Zhang, S.-Y. Xu, I. Belopolski, Z. Yuan, Z. Lin, B. Tong, G. Bian, N. Alidoust, C.-C. Lee, S.-M. Huang, T.-R. Chang, G. Chang, C.-H. Hsu, H.-T. Jeng, M. Neupane, D. S. Sanchez, H. Zheng, J. Wang, H. Lin, C. Zhang *et al.*, *Nat. Commun.* **7**, 10735 (2016).
- [9] Q. Li, D. E. Kharzeev, C. Zhang, Y. Huang, I. Pletikosić, A. V. Fedorov, R. D. Zhong, J. A. Schneeloch, G. D. Gu, and T. Valla, *Nat. Phys.* **12**, 550 (2016).
- [10] C. Y. Guo, F. Wu, Z. Z. Wu, M. Smidman, C. Cao, A. Bostwick, C. Jozwiak, E. Rotenberg, Y. Liu, F. Steglich, and H. Q. Yuan, *Nat. Commun.* **9**, 4622 (2018).
- [11] H. Li, H.-W. Wang, H. He, J. Wang, and S.-Q. Shen, *Phys. Rev. B* **97**, 201110(R) (2018).
- [12] R. Singha, S. Roy, A. Pariari, B. Satpati, and P. Mandal, *Phys. Rev. B* **98**, 081103(R) (2018).
- [13] S. Liang, J. Lin, S. Kushwaha, J. Xing, N. Ni, R. J. Cava, and N. P. Ong, *Phys. Rev. X* **8**, 031002 (2018).
- [14] N. Kumar, S. N. Guin, C. Felser, and C. Shekhar, *Phys. Rev. B* **98**, 041103(R) (2018).
- [15] O. Pavlosiuk, D. Kaczorowski, and P. Wiśniewski, *Phys. Rev. B* **99**, 125142 (2019).
- [16] S. Chadov, X. Qi, J. Kübler, G. H. Fecher, C. Felser, and S. C. Zhang, *Nat. Mater.* **9**, 541 (2010).
- [17] W. Al-Sawai, H. Lin, R. S. Markiewicz, L. A. Wray, Y. Xia, S.-Y. Xu, M. Z. Hasan, and A. Bansil, *Phys. Rev. B* **82**, 125208 (2010).
- [18] Z. Hou, Y. Wang, E. Liu, H. Zhang, W. Wang, and G. Wu, *Appl. Phys. Lett.* **107**, 202103 (2015).
- [19] See Supplemental Material at <http://link.aps.org/supplemental/10.1103/PhysRevB.103.205127> for results of material characterization, raw data of Hall resistance, electrical resistivity measurements, heat capacity measurement and analysis, three-band model fitting to Hall resistivity, WAL and CMA terms fitting to MR, extended electronic structure calculations, and supplemental references [41–48].
- [20] J. Rodriguez-Carvajal, *Physica B* **192**, 55 (1993).
- [21] K. Koepf and H. Eschrig, *Phys. Rev. B* **59**, 1743 (1999).
- [22] H. Eschrig, K. Koepf, and I. Chaplygin, *J. Solid State Chem.* **176**, 482 (2003).
- [23] J. P. Perdew, K. Burke, and M. Ernzerhof, *Phys. Rev. Lett.* **77**, 3865 (1996).
- [24] E. D. Mun, S. L. Bud'ko, C. Martin, H. Kim, M. A. Tanatar, J.-H. Park, T. Murphy, G. M. Schmiedeshoff, N. Dilley, R. Prozorov, and P. C. Canfield, *Phys. Rev. B* **87**, 075120 (2013).
- [25] Z. Hou, W. Wang, G. Xu, X. Zhang, Z. Wei, S. Shen, E. K. Liu, Y. Yao, Y. Chai, Y. Sun, X. Xi, W. Wang, Z. Liu, G. Wu, and X.-X. Zhang, *Phys. Rev. B* **92**, 235134 (2015).
- [26] O. Pavlosiuk, D. Kaczorowski, and P. Wiśniewski, *Phys. Rev. B* **94**, 035130 (2016).
- [27] H. Xiao, T. Hu, W. Liu, Y. L. Zhu, P. G. Li, G. Mu, J. Su, K. Li, and Z. Q. Mao, *Phys. Rev. B* **97**, 224511 (2018).
- [28] H. Chi, C. Zhang, G. Gu, D. E. Kharzeev, X. Dai, and Q. Li, *New J. Phys.* **19**, 015005 (2017).
- [29] C. L. Zhang, Z. Yuan, Q. D. Jiang, B. Tong, C. Zhang, X. C. Xie, and S. Jia, *Phys. Rev. B* **95**, 085202 (2017).
- [30] M. N. Ali, L. Schoop, J. Xiong, S. Flynn, Q. Gibson, M. Hirschberger, N. P. Ong, and R. J. Cava, *Europhys. Lett.* **110**, 67002 (2015).
- [31] E. Sondheimer, *Proc. R. Soc. London A* **268**, 100 (1962).
- [32] A. B. Pippard, *Magnetoresistance in Metals* (Cambridge University Press, Cambridge, 2009).
- [33] J. Hu, M. M. Parish, and T. F. Rosenbaum, *Phys. Rev. B* **75**, 214203 (2007).
- [34] X. Dai, H.-Z. Lu, S.-Q. Shen, and H. Yao, *Phys. Rev. B* **93**, 161110(R) (2016).
- [35] H.-Z. Lu and S.-Q. Shen, *Phys. Rev. B* **92**, 035203 (2015).
- [36] H. J. Kim, K. S. Kim, J. F. Wang, M. Sasaki, N. Satoh, A. Ohnishi, M. Kitaura, M. Yang, and L. Li, *Phys. Rev. Lett.* **111**, 246603 (2013).
- [37] P. Li, C. Zhang, Y. Wen, L. Cheng, G. Nichols, D. G. Cory, G.-X. Miao, and X.-X. Zhang, *Phys. Rev. B* **100**, 205128 (2019).
- [38] R. Majumder and S. K. Mitró, *RSC Adv.* **10**, 37482 (2020). We cite this paper because it concerns the same compound, but we found that it contains severe internal inconsistency. It seems that the same calculation yielded an electronic band structure typical for a zero-gap semiconductor, a finite density of states at the Fermi level (typical for semimetal), and a Fermi surface enclosing a large volume (typical for metal).
- [39] K. Synoradzki, K. Ciesielski, I. Veremchuk, H. Borrmann, P. Skokowski, D. Szymański, Y. Grin, and D. Kaczorowski, *Materials* **12**, 1723 (2019).
- [40] C. Shekhar, N. Kumar, V. Grinenko, S. Singh, R. Sarkar, H. Luetkens, S.-C. Wu, Y. Zhang, A. C. Komarek, E. Kampert, Y. Skourski, J. Wosnitzer, W. Schnelle, A. McCollam, U. Zeitler, J. Kübler, B. Yan, H.-H. Klauss, S. S. P. Parkin, and C. Felser, *Proc. Natl. Acad. Sci. USA* **115**, 9140 (2018).
- [41] Y. Nakajima, R. Hu, K. Kirshenbaum, A. Hughes, P. Syers, X. Wang, K. Wang, R. Wang, S. R. Saha, D. Pratt, J. W. Lynn, and J. Paglione, *Sci. Adv.* **1**, e1500242 (2015).
- [42] O. Pavlosiuk, D. Kaczorowski, and P. Wiśniewski, *Sci. Rep.* **5**, 9158 (2015).

- [43] O. Pavlosiuk, D. Kaczorowski, X. Fabrèges, A. Gukasov, and P. Wiśniewski, *Sci. Rep.* **6**, 18797 (2016).
- [44] N. P. Butch, P. Syers, K. Kirshenbaum, A. P. Hope, and J. Paglione, *Phys. Rev. B* **84**, 220504(R) (2011).
- [45] Y. Wu, N. H. Jo, M. Ochi, L. Huang, D. Mou, S. L. Bud'ko, P. C. Canfield, N. Trivedi, R. Arita, and A. Kaminski, *Phys. Rev. Lett.* **115**, 166602 (2015).
- [46] Y. Zhang, C. Wang, L. Yu, G. Liu, A. Liang, J. Huang, S. Nie, X. Sun, Y. Zhang, B. Shen, J. Liu, H. Weng, L. Zhao, G. Chen, X. Jia, C. Hu, Y. Ding, W. Zhao, Q. Gao, C. Li *et al.*, *Nat. Commun.* **8**, 15512 (2017).
- [47] G. Ding, G. Y. Gao, L. Yu, Y. Ni, and K. Yao, *J. Appl. Phys.* **119**, 025105 (2016).
- [48] K. Kaur, S. Dhiman, and R. Kumar, *Phys. Lett. A* **381**, 339 (2017).